Chapter 5

Channel Modeling And Capacity Analysis For Nanoscale Communications And Networking

Authors:
V. Musa[1,2], G. Piro[1,2], P. Bia[3], L. A. Grieco[1,2], D. Caratelli[4], L. Mescia[1,2], G. Boggia[1,2]

Affiliations:
[1] DEI, Politecnico di Bari. Via Orabona 4, Bari, Italy
[2] CNIT, Consorzio Nazionale Interuniversitario per le Telecomunicazioni
[3] Design Solution Department, Elettronica S.p.A., Via Tiburtina Valeria Km 13,700, 00131 Rome, Italy
[4] The Antenna Company Nederland B.V., High Tech Campus, Eindhoven, The Netherlands

Contents

5.1 Introduction

The innovation process triggered by nanotechnology is rapidly concretizing the idea to deploy network architectures at the nanoscale, made up by integrated devices with size ranging from one to few hundred of nanometers. These devices are able to interact with each other by using novel communication mechanisms, thus enabling new pioneering applications in Information and Communication Technologies (ICT), biomedical, industrial, and military domains [1]. Accordingly, the time is ready to conceive innovative networking methodologies, protocols, and algorithms, which properly embrace the main facets of nanoscale communication systems, while fulfilling the requirements of enabled applications. However, at this embryonic stage of the research, any activity focusing on nanoscale networking should ground its roots to solid studies that carefully describe how the information is really exchanged between transmitter and receiver at the nanoscale. In this context, channel modeling and capacity analysis become key aspects to investigate before deeply proceeding in this direction of research.

With reference to the healthcare domain, for instance, nanoscale communications and networking could enable advanced immune systems, bio-hybrid implant solutions, drug delivering systems, pervasive health monitoring, and genetic engineering [2] [3]. It is foreseen, in fact, that biomedical nano-devices can be implanted, ingested, or worn by humans for collecting diagnostic information (e.g., the presence of sodium, glucose, and/or other ions in blood, cholesterol, as well as cancer biomarkers and other infectious agents) and for tuning medical treatments (e.g., insulin and other drugs injection through under-skin actuators). In this context, while graphene-based nano-antennas generating electromagnetic waves in the Terahertz band (i.e., from 0.1 THz to 10 THz) make the communication feasible at the nanoscale and in human tissues [4], the actual physical transmission rates and communication ranges are significantly influenced by many aspects characterizing the communication process [5]. The most important ones include propagation losses, the dispersive nature of the communication channel, the molecular noise, the adopted transmission techniques, and the positions of both transmitter and receiver.

Starting from these premises, this book chapter aims to investigate physical transmission rates and communication ranges reachable in human tissues, starting from the formulation of a sophisticated channel model that takes into account the frequency and spatial dependence of the skin permittivity.

First, the communication channel is modeled as a stratified medium, composed by stratum corneum, epidermis, dermis, and hypodermis. Here, the electromagnetic field and the Poynting vector are calculated by using the Finite-Difference Time-Domain (FDTD) technique, able to directly solve the Maxwell's equations in time domain. Second, starting from the aforementioned channel model, the total path loss (expressed as the sum of spreading and absorption path loss), the molecular noise temperature, and the noise power spectral density are evaluated as a function of the communication frequency and the distance between transmitter and receiver. To make the study more general as possible, two configurations are considered. The first one, namely bottom-up, assumes that the transmitter is implanted in the human body and the receiver is directly positioned on the skin surface. On the contrary, the second configuration, namely top-down, investigates the communication process when the position of both transmitter and receiver are inverted with respect to the previous case. Third, by considering three different transmission mechanisms based on the Time Spread On-Off Keying (TS-OOK) modulation scheme [4] [6] (namely flat, pulse-based, and optimal), the Signal-to-Noise Ratio (SNR) is evaluated as a function of communication frequency and the distance between transmitter and receiver. All the obtained results are finally processed for studying the upper bound of physical transmission rates and communication ranges achievable in human tissues when the reference communication bandwidth is delimited to the set of frequencies spanning from 0.5 THz to 1.5 THz.

The proposed study demonstrates that a physical data rate in the order of Tbps can be only reached for transmission ranges less than 2 mm. When the distance between transmitter and receiver exceeds 9 mm, communication capabilities are extremely impaired (i.e., the physical data rate tends to be lower than 1 bps). Moreover, higher performance is measured for the bottom-up configuration, where inner layers of the communication medium produce lower levels of attenuation of the propagating signal.

The rest of this book chapter is organized as in the following. Section 5.2 presents the channel model formulated for the stratified media stack describing human tissues. Section 5.3 describes the investigated transmission techniques. Section 5.4 discusses the SNR measured in the frequency domain and illustrates physical transmission rates and communication ranges achievable in human tissues as a function of transmission techniques, distance and position of both transmitter and receiver. Finally, Section 5.5 draws the conclusions.

5.2 Channel models for nanoscale communications in human tissues

The modeling of the Pulsed Electric Field (PEF) propagation in biological tissues is a subject of increasing research activities since they are used in a number of applications in bioelectrics, a new interdisciplinary field combining knowledge of electromagnetic principles and theory, modeling and simulations, physics, material science, cell biology, and medicine [7, 8, 9]. Several studies are focused on the use of PEFs for reversible or irreversible electroporation to achieve selective killing of cancer cells, tissue ablation, gene therapy, and DNA based vaccination [10, 11]. Moreover, recent applications employing PEFs technology include medical implant communication service, wireless medical telemetry service, body area networks, nanonetworks in a living biological environment, in-body electromagnetic communications [12, 13, 14, 15].

All these technologies involve the interaction of electromagnetic fields with complex dielectric materials. For instance, in the contest of the in-body communications among the nano-devices the right evaluation of the network performance in term of data rate and transmission range needs of an accurate modeling of the electromagnetic field propagation inside human tissues. As a result, the development of theoretical models and computational techniques to determine the propagation properties of electromagnetic pulses is fundamental to gain insight into the several phenomena occurring within complex dielectric materials subject to an imposed PEFs. In fact, the complexity of the structure and composition of such matter produces a time-domain response generally non-symmetric and markedly different from that of dielectric media modeled by the simple dielectric response relationships. As a consequence, the dielectric response in the frequency domain usually requires empirical models exhibiting fractional powers of the angular frequency $j\omega$. Due to this, the solution of the Maxwell's equations in the time domain is not trivial since it involves the concept of fractional derivatives [16].

5.2.1 Dielectric dispersion model

The interaction between PEF and biological tissues takes place in different relaxation processes such as reorientation of dipolar molecules, interfacial polarization, ionic diffusion due to ions of different signs of charges, conduc-

tivity of surface cell structures, motion of the molecules, the non-spherical shape as well as in different resonant phenomena due to molecular, atomic or electronic vibrations. Their resulting behavior causes a frequency dispersion pattern of permittivity and conductivity [17].

The analytical theory modeling the frequency-dependent permittivity of dielectric media is based on the response function through the following relation

$$\phi(\omega) = \frac{\varepsilon(\omega) - \varepsilon_\infty}{\Delta\varepsilon} \tag{5.1}$$

where $\varepsilon(\omega)$ is the frequency-dependent complex relative permittivity, ε_∞ is asymptotic relative permittivity, $\Delta\varepsilon$ is the dielectric strength. An useful technique allowing the reproduction of the experimental spectra $\varepsilon(\omega)$ by adjusting some free parameters of a mathematical expression is based on the use of an empirical dielectric function model in conjunction with nonlinear least square optimization. Using this method, the empirical response functions exhibiting a broad distribution of relaxation times has been proposed [18]

$$\phi\left(\omega\right) = \frac{1}{\left[\left(j\omega\tau\right)^{\gamma} + \left(j\omega\tau\right)^{\alpha}\right]^{\beta}} \tag{5.2}$$

where the adjusting parameters $0 \leq \alpha, \beta, \gamma \leq 1$ account for shape and behavioral features of the permittivity function. The Eq. (5.2) strongly deviate from the conventional Debye law ($\gamma = 0$, $\alpha = \beta = 1$) and it can be used to reproduce other empirical response functions as Cole-Cole ($\gamma = 0$, $\beta = 1$), Cole-Davidson ($\gamma = 0$, $\alpha = 1$) and Havriliak-Negami ($\gamma = 0$) . However, its effectiveness may fall when the dielectric response of more complex materials having heterogeneous, inhomogeneous and disordered structure at both microscopic and mesoscopic scales has to be modeled. To overcome this limitation and to provide an extended model parametrization as well as a better and flexible fitting of the experimental data over broad frequency ranges a general fractional polynomial series approximation has been proposed by the authors [7, 8, 19]

$$\phi\left(\omega\right) = \sum_{i=1}^{N} \frac{\Delta\varepsilon_i}{\mathcal{Q}_i} \tag{5.3}$$

and

$$\mathcal{Q}_i = \sum_{k=0}^{K} b_{k,i} \left(j\omega\tau_{k,i}\right)^{\beta_{k,i}} \tag{5.4}$$

where $b_{k,i}, \beta_{k,i}$ denote suitable real-valued parameters chosen so that i) to avoid model singularities, ii) to fulfill the consistency of the representation, and iii) to ensure the passivity condition. Applying a dedicated optimization algorithm employing a suitable relative error function, the free parameters $b_{k,i}, \beta_{k,i}, \tau_{k,i}, K, N$ can be evaluated [20]. This method is versatile because its capability to deal with every data, it can reproduce fine details, and it proved to feature superior effectiveness in terms of convergence rate and accuracy.

5.2.2 FDTD modeling

The Finite Difference Time Domain (FDTD) technique is a well-known numerically robust and appropriate method for the computer technology of today. It is well know that the solution of Maxwell's equations in dispersive media is a stiff problem and the development of FDTD methods to study the transient wave propagation in such media is an area of active interest. In detail, the FDTD implementation of the dispersion characteristics described by Eq. (5.3)-(5.4) is difficult and it requires special treatments. However, the nature of the fractional order operators modeling the dielectric response described by Eq. (5.4) enables its incorporation into time-domain Maxwell's equations using a non-local pseudo-differential operators of non-integer order.

For a nonmagnetic and isotropic dispersive dielectric material with response function described by Eq. (5.4) the frequency-domain Maxwell's equations can be written as

$$\nabla \times \mathbf{H} = j\omega\varepsilon_0 \left(\varepsilon_\infty - j\frac{\sigma}{\omega\varepsilon_0} \right) \mathbf{E} + \sum_{i=1}^{N} \mathbf{J}_i \tag{5.5}$$

$$\nabla \times \mathbf{E} = -j\omega\mu_0 \mathbf{H} \tag{5.6}$$

where σ is the static conductivity, $\mathbf{H}$ is the magnetic field, and the pth term of the auxiliary displacement current density $\mathbf{J} = \sum_{i=1}^{N} \mathbf{J}_i$ is given by

$$\mathbf{J}_p = j\omega\varepsilon_0 \frac{\Delta\varepsilon_p}{\mathcal{Q}_p} \mathbf{E} \tag{5.7}$$

where

$$\mathcal{Q}_p = \sum_{k=0}^{K} b_{k,p} \left(j\omega\tau_{k,p} \right)^{\beta_{k,p}} \tag{5.8}$$

Taking the inverse Fourier transform of Eq. (5.7) and following the procedure well illustrated in [7, 21, 22, 23], it is possible to find the following updating equations, in time domain, for the magnetic and electric fields as well as for the displacement current density:

$$\boldsymbol{\mathcal{H}}|^{m+1} = \boldsymbol{\mathcal{H}}|^{m} - \frac{\Delta t}{\mu_0} \nabla \times \boldsymbol{\mathcal{E}}|^{m+1/2} \tag{5.9}$$

$$\boldsymbol{\mathcal{E}}|^{m+1/2} = \frac{2\varepsilon_0\varepsilon_\infty - \sigma\Delta t}{2\varepsilon_0\varepsilon_\infty + \sigma\Delta t} \boldsymbol{\mathcal{E}}|^{m-1/2} + \frac{2\Delta t}{2\varepsilon_0\varepsilon_\infty + \sigma\Delta t} \left[\nabla \times \boldsymbol{\mathcal{H}}|^{m} - \frac{1}{2} \sum_{i=1}^{N} \left(\boldsymbol{\mathcal{J}}_i|^{m-1/2} + \boldsymbol{\mathcal{J}}_i|^{m+1/2} \right) \right] \tag{5.10}$$

$$\begin{aligned} \left(\varepsilon_\infty + \frac{\sigma\Delta t}{2\varepsilon_0} \right) \frac{C^{(\beta_{k,p})}}{\Delta\varepsilon_p} \boldsymbol{\mathcal{J}}_p|^{m+1/2} + \frac{1}{2} \sum_{i=1}^{N} \boldsymbol{\mathcal{J}}_i|^{m+1/2} \\ = \nabla \times \boldsymbol{\mathcal{H}}|^{m} - \sigma \nabla \times \boldsymbol{\mathcal{E}}|^{m-1/2} + \\ - \frac{1}{2} \sum_{i=1}^{N} \boldsymbol{\mathcal{J}}_i|^{m-1/2} - \frac{1}{\Delta\varepsilon_p} \left(\varepsilon_\infty + \frac{\sigma\Delta t}{2\varepsilon_0} \right) \\ \left[\sum_{k=0}^{K_i} \sum_{s=1}^{\nu} \xi_{k,s}^{(\beta_{k,p})} \boldsymbol{\mathcal{J}}_p|^{m-s+1/2} + \right. \\ \left. + \sum_{k=0}^{K_i} \sum_{s=1}^{\nu} \sum_{q=1}^{Q_{k,\alpha_p}} \eta_{k,s,q}^{(\beta_{k,p})} \psi_q^{(\beta_{k,p})} \Big|^{m-s} \right] \end{aligned} \tag{5.11}$$

With the aim to suitably bound the computational domain, a dedicated uniaxial perfect matched layer (UPML) boundary conditions was derived in combination with the basic time-marching scheme accounting for the electrical conductivity and the multirelaxation characteristics of the dielectric material under analysis. In particular, the developed approach combines the stretched auxiliary electric field and density current vectors with the fractional derivative equation describing the dispersion properties of the medium. In particular, by following the mathematical procedure well detailed in [7, 21] the update equations for both electric and magnetic field within the UPML

termination can be written as

$$\boldsymbol{\mathcal{E}}\big|^{m+1/2} = \frac{2\varepsilon_0\kappa_x - \sigma_x\Delta t}{2\varepsilon_0\kappa_x + \sigma_x\Delta t}\,\boldsymbol{\mathcal{E}}\big|^{m-1/2} + \\ + \frac{2\varepsilon_0}{2\varepsilon_0\kappa_x + \sigma_x\Delta t}\left(\mathbf{e}\big|^{m+1/2} - \mathbf{e}\big|^{m-1/2}\right) \quad (5.12)$$

and

$$\boldsymbol{\mathcal{H}}\big|^{m+1} = \frac{2\varepsilon_0\kappa_x - \sigma_x\Delta t}{2\varepsilon_0\kappa_x + \sigma_x\Delta t}\,\boldsymbol{\mathcal{H}}\big|^{m} + \\ - \frac{2Y_0\Delta t}{2\varepsilon_0\kappa_x + \sigma_x\Delta t}\,\nabla\times\boldsymbol{\mathcal{E}}\big|^{m+1/2} \quad (5.13)$$

where Y_0 is the wave admittance in free space, σ_x, κ_x are the UPML material parameters, and $\mathbf{e}$ is the auxiliary electric field vector.

5.2.3 Electromagnetic simulations

Most recent studies of electromagnetic channel at the Terahertz band for the body-centric nano-networks treat the skin tissue as a homogeneous semi-infinite medium resulting by the binary mixture of water and biological background material (bound water, keratin, lipids and collagen) [1, 24]. In general, the skin is a mosaic in which layers of laminated, inhomogeneous cell structure pile up on top of one another. As a result, it can be modeled as a stratified media stack consisting of stratum corneum (SC), epidermis (E), dermis (D) and hypodermis (HYP) (see figure 1). The SC contains corneocytes embedded in a lipid matrix. The corneocyte does not contain a nucleus as well as the extracellular matrix mainly consists of lipids and proteins and very little bound water. So, the total water volume fraction in the SC is 0.15-0.25, while 90% of the water is contained within the corneocyte. The SC thickness depends on the body site and it is typically tens of micrometers. In our modeling the SC is 20 μm thick [25, 26, 27, 28]. However, due to the high lipid and protein and low water content the SC differs significantly from the epidermis layer. In fact, the epidermis mainly consists of keratinocytes and it is characterized by an overall water volume fraction of about 0.7, equally distributed among intra- and extracellular space. The dermis is the more complex and heterogeneous layer. In fact, the upper 10% consists of a dense collagen network and blood while the major part is mainly composed by ir-

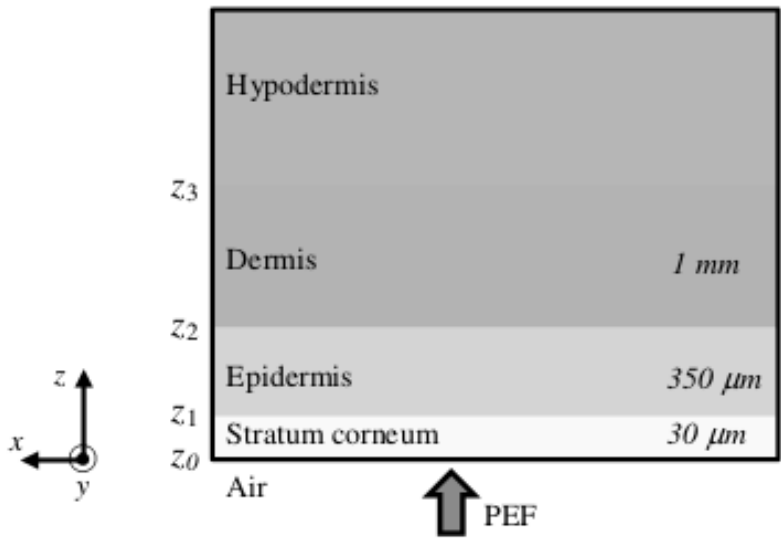

Figure 5.1: The considered layered structure describing human tissues.

regular connective tissue, lymphatic vessels, nerves, blood vessels, stromal cells (fibroblasts) and other cellular components (macrophages or plasma) [29, 30]. Collagen is a major component embedded in the dermal matrix. In addition to collagen and elastin the extracellular space is mainly composed of glycosaminoglycans, gelatin and sugars embedded in water. Finally, the hypodermis (HYP) mainly consists of white fat cells and adipocytes building the subcutaneous fat. The intracellular fat forms a spherical droplet having a volume fraction of about 0.9. Thus, the aqueous phase volume fraction is only 0.1.

Considering the complexity of the skin and with the aim to provide a more detailed modeling of the electromagnetic field propagation inside the skin at the Terahertz band, a non-homogeneous and dispersive model based on stratified media stack illustrated in figure 1 has been taken into account. The dielectric properties of stratum corneum, epidermis, dermis and fat in a desired frequency range, as well as the thickness of each layer have been calculated by considering experimental results reported in the literature [25, 26, 27, 28]. In particular, the frequency-domain permittivity function has

been designed by minimizing the following error function:

$$\text{err} = \frac{\int_{\omega_{\min}}^{\omega_{\max}} |\varepsilon_{\exp}(\omega) - \varepsilon(\omega)|^2 \mathrm{d}\omega}{\int_{\omega_{\min}}^{\omega_{\max}} |\epsilon_{\exp}(\omega)|^2 \mathrm{d}\omega} \leq \delta, \tag{5.14}$$

where δ is the maximum tolerable error, $\epsilon_{\exp}$ is the measured permittivity, and ϵ represents the general dielectric response. The set of parameters related to each layer have been reported in Table 5.1. These values have been obtained by using the relationship

$$\varepsilon(\omega) = \varepsilon_\infty + \sum_{i=1}^{2} \frac{\Delta\varepsilon_i}{1 + \sum_{k=1}^{2} b_{i,k} \left(j\omega\tau_{i,k}\right)^{\beta_{i,k}}} - j\frac{\sigma}{\omega\varepsilon_0} \tag{5.15}$$

in a bandwidth ranging from 0.5 THz to 1.5 THz.

Table 5.1: Parameters of the recovered complex permittivity function

Tissue	$b_{1,1}$	$b_{1,2}$	$b_{2,1}$	$b_{2,2}$	$\beta_{1,1}$	$\beta_{1,2}$	$\beta_{2,1}$	$\beta_{2,2}$	$\Delta\varepsilon_1$	$\Delta\varepsilon_1$	σ (S/m)	ϵ_∞
Stratum Corneum	10.11	-9.25	–	–	0.9	0.88	–	–	12.22	–	0.035	2.4
Epidermis	1.04	-0.02	–	–	0.9	0.03	–	–	89.61	–	0.01	3
Dermis	0.88	-0.17	10	-9.1	0.77	0.01	0.9	0.88	5.96	380.4	0.1	4
Hypodermis	0.89	-0.19	0.96	-0.05	0.81	0.01	0.8	0.04	1.14	9.8	0.035	2.5

The electromagnetic source is a plane wave propagating along the positive z-direction with electric field linearly polarized along the x-axis. In particular, the time-domain signal source is an electric current density $\boldsymbol{\mathcal{J}}_0$ placed at a given position $z = \overline{z}$ inside the computational domain:

$$\boldsymbol{\mathcal{J}}_0(z,t) = \exp\left\{-a^2\left(t - \frac{2}{a}\right)^2\right\} \sin\left[2\pi f_0\left(t - \frac{4}{a}\right)\right] \delta\left(z - \overline{z}\right) \hat{\mathbf{x}}, \tag{5.16}$$

where the parameters $f_0 = 1$ THz and $1/a = 100$ fs have been selected to achieve a bandwidth from 0.5 THz to 1.5 THz. The considered time and spatial steps are $\Delta t = 10$ fs and $\Delta z = 6$ μm, respectively. The validation

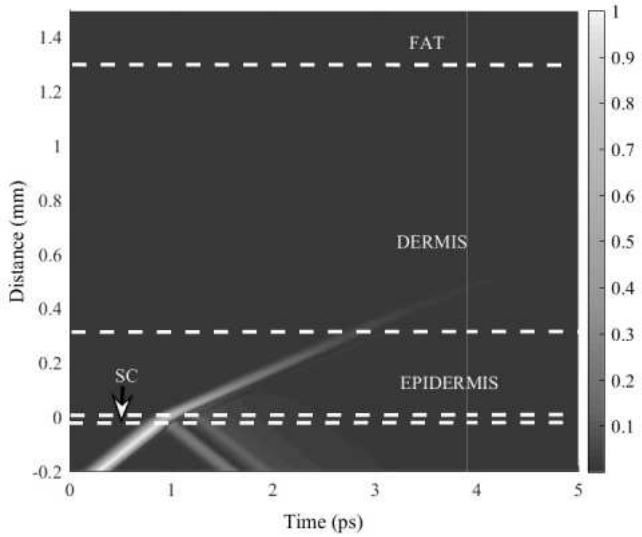

Figure 5.2: Modulus of the normalized space-time distribution of electric field.

of the developed numerical procedure has been illustrated in detail in our previous papers [7, 8, 19, 21, 31].

To provide a further insight, the Poynting vector, $\mathbf{S}(\omega, z)$, is also reported in Figure 5.4. In particular, it has been calculated as:

$$\mathbf{S}(\omega, z) = \mathbf{E} \times \mathbf{H}^*,$$

$\mathbf{E}$ and $\mathbf{H}$ are the Fourier transform of $\boldsymbol{\mathcal{E}}$ and $\boldsymbol{\mathcal{H}}$, respectively.

In Figures 5.2,5.3 and 5.4, it can be observed the multiple reflected waves generated by the stratified media stack as well as the main reflection phenomenon occurring at the air-skin interface. Moreover, it is evident the wave pulse spreading due to the propagation inside the dispersive biological media.

5.2.4 Path loss and noise models

To deal with nanoscale communications and networking, it is important to know how the signal propagates across the medium. Starting from the FDTD model and related results reported above, this Section develops an accurate channel model, taking into account two possible configurations. The first

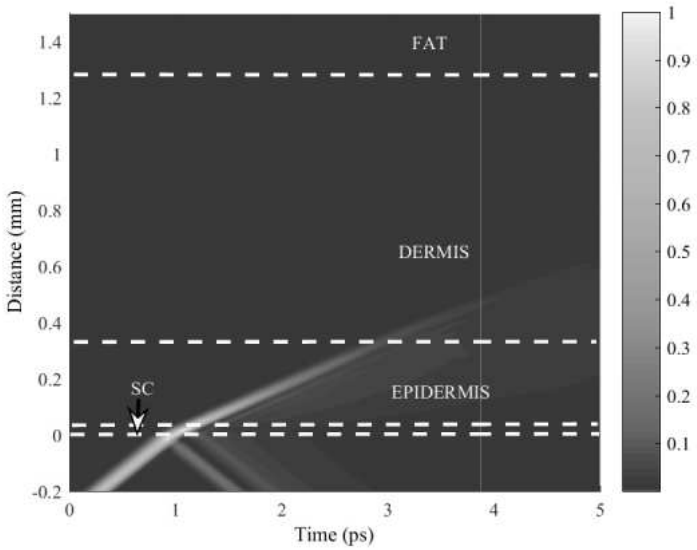

Figure 5.3: Modulus of the normalized space-time distribution of magnetic field.

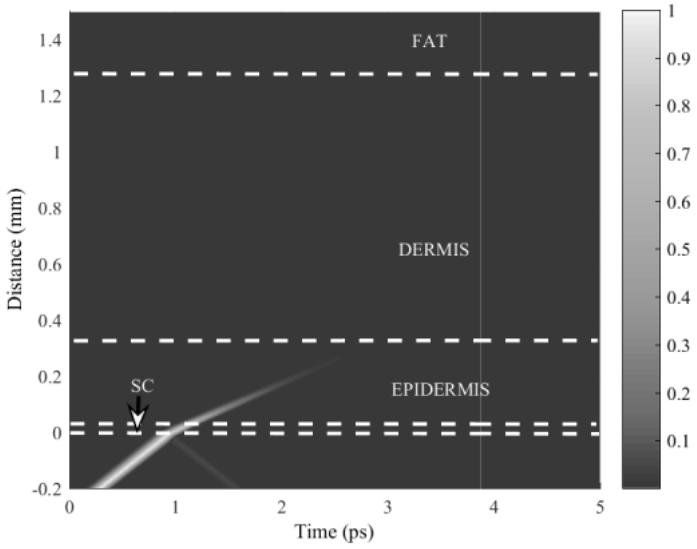

Figure 5.4: Modulus of the normalized space-time distribution of Poynting vector.

one refers to the bottom-up communication, where it is assumed that the transmitter is implanted and the receiver is positioned outside the human body (but attached to the skin). The second one refers to the top-down configuration, where the position of transmitter and receiver is inverted with respect to the previous case. The resulting channel model embraces absorption path loss, spreading path loss, molecular noise temperature, and noise power spectral density. Such models will be used in the next Section for evaluating the communication capacity as a function of the distance between transmitter and receiver.

5.2.4.1 Absorption path loss

When an electromagnetic wave propagates through the medium, several molecules are excited and start to vibrate. In this case, part of the energy carried by the electromagnetic wave is lost or converted to kinetics energy [1]. The absorption path loss or molecular loss, i.e., $A_{abs}(\omega, z)$, describes the attenuation produced by the vibration of molecules as a function of both distance between transmitter and receiver, d, and communication frequency, f, that is:

$$A_{abs}(\omega, z)\Big|_{\text{dB}} = 10 \log \frac{\boldsymbol{S}(\omega, z)}{\boldsymbol{S}(\omega, z_0)} = 10k(\omega)d \log e, \tag{5.17}$$

where $\boldsymbol{S}$ is the Poynting vectors, z_0 is the z-coordinate of the reference section, $d = z - z_0$ is the considered path length and $k(\omega)$ is the medium absorption coefficient.

Given the stratified channel model reported in Figure 5.1, the absorption path loss offered by human tissues in the bandwidth from 0.5 THz to 1.5 THz is shown in Figure 5.5. Without loss of generality, the reported results consider the top-down configuration. The absorption path loss clearly appears as a frequency-selective attenuation, which grows up when both transmission range and communication frequency increase.

5.2.4.2 Spreading path loss

The spreading path loss, i.e., $A_{spread}(\omega, z)$, refers to the attenuation due to the expansion of an electromagnetic wave propagating through a given medium.

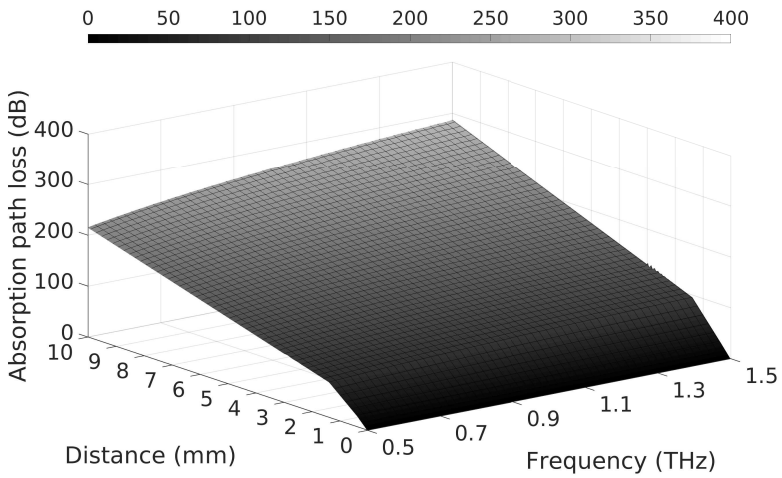

Figure 5.5: Absorption path loss as a function of frequency and transmission range, evaluated for the top-down configuration.

It is defined as:

$$A_{spread}(\omega, z)\Big|_{\text{dB}} = 20\log\left(4\pi \int_{z_0}^{z} \frac{dz}{\lambda_g(\omega, z)}\right), \tag{5.18}$$

where λ_g takes into account the stratified medium and depends on the distance from the air-skin interface. Specifically, λ_g can be expressed as:

$$\lambda_g(\omega, z) = \begin{cases} \lambda_{g,1}(\omega, z) & 0 \leq z \leq z_1 \\ \lambda_{g,2}(\omega, z) & z_1 \leq z \leq z_2 \\ \lambda_{g,3}(\omega, z) & z_2 \leq z \leq z_3 \\ \lambda_{g,4}(\omega, z) & z \geq z_3, \end{cases} \tag{5.19}$$

where

$$\lambda_{g,k} = \frac{\lambda_0}{\sqrt{\dfrac{\varepsilon'_k}{2}\left[\sqrt{1 + \left(\dfrac{\varepsilon''_k}{\varepsilon'_k} + \dfrac{\sigma_k}{f\epsilon_0\varepsilon'_k}\right)^2} + 1\right]}} \quad k = 1, 2, 3, 4 \tag{5.20}$$

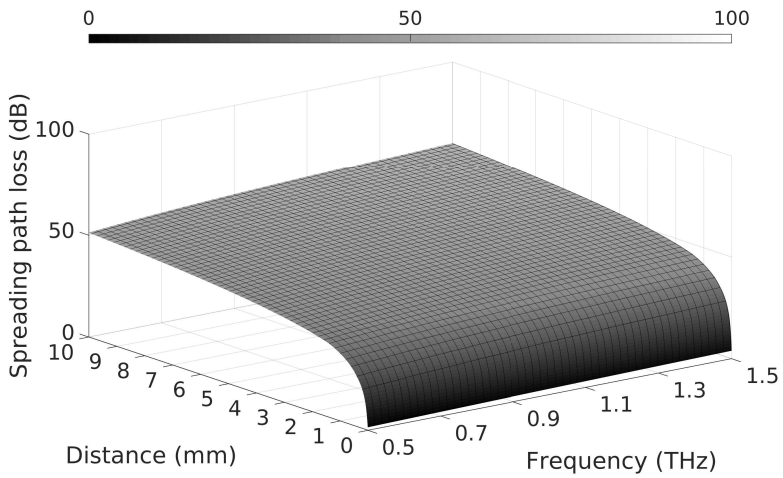

Figure 5.6: Spreading path loss as a function of frequency and transmission range, evaluated for the top-down configuration.

is the wavelength of the propagating wave within the k-th lossy medium, while λ_0 is the free-space wavelength.

Figure 5.6 depicts the spreading path loss in human tissues as a function of the transmission range and the communication frequency, evaluated for the top-down configuration. In general, the spreading path loss registers considerably high values at the nanoscale. But, in this specific use case, it appears negligible with respect to the level of attenuation provided by the absorption path loss.

5.2.4.3 Total path loss

The total signal path loss, i.e., $A(\omega, z)$, defines the total level of attenuation offered to the signal that propagates across the medium. According to [1], it jointly takes care about the absorption path loss due to the absorption of human tissues, i.e., $A_{abs}(\omega, z)$, and the spreading path loss generated by the expansion of waves in human body, i.e., $A_{spread}(\omega, z)$. Thus, $A(\omega, z)$ can be defined as:

$$A(\omega, z)\Big|_{\text{dB}} = A_{spread}(\omega, z)\Big|_{\text{dB}} + A_{abs}(\omega, z)\Big|_{\text{dB}}. \tag{5.21}$$

Figure 5.7 shows the total path loss as a function of the distance between

transmitter and receiver and the communication frequency, by taking into account both top-down and bottom-up configurations. Generally, the total path loss grows up when the communication frequency and the transmission range increase. However, the comparison between Figure 5.7 (a) and Figure 5.7 (b) shows how the outer skin layers introduce higher attenuation levels than the inner ones. Moreover, by comparing Figure 5.7 (a) with both Figure 5.5 and Figure 5.6, it is evident how the total path loss is mainly influenced by the molecular absorption, which generates a loss up to 6 times higher than the one introduced by the expansion phenomenon. Just to provide an example, with reference to the considered communication bandwidth, the maximum value of the spreading path loss is 60.3 dB, while the absorption path loss registers a maximum value equal to 287.2 dB. Moreover, reported results fully confirm that the Terahertz band is strongly frequency-selective: in fact, the propagation loss significantly increases with both communication frequency and transmission range.

5.2.4.4 Molecular noise temperature

Molecular absorption also generates the molecular noise. Specifically, the equivalent molecular noise temperature is computed as:

$$T_{eq}(\omega, z) = T_0 \varepsilon(\omega, z) = T_0 \left[1 - \frac{\boldsymbol{S}(\omega, z)}{\boldsymbol{S}(\omega, z_0)}\right], \tag{5.22}$$

where T_0 is the reference temperature, equal to normal body temperature (i.e., $T_0 = 310K$), $\boldsymbol{S}(\omega, z)$ is the Poynting vector, and $\varepsilon(\omega, z)$ is the channel emissivity.

As depicted in Figure 5.8, the molecular noise temperature changes with communication frequency and transmission distance. Indeed, the internal vibrations of the medium molecules absorb the propagating electromagnetic field and convert the carried energy to kinetic energy (first) and heat (then). In this context, the emissivity of the channel could be expressed as a function of the absorption path loss and could be set equal to 1-$\boldsymbol{S}(\omega, z)/\boldsymbol{S}(\omega, z_0)$.

To provide further insight, both top-down and bottom-up configurations are taken into account. As already observed, the inner tissue layers register lower attenuation levels. Consequently, the molecular noise temperature increases slower when the bottom-up configuration is considered. On the other hand, in both configurations it is important to note that, at the level

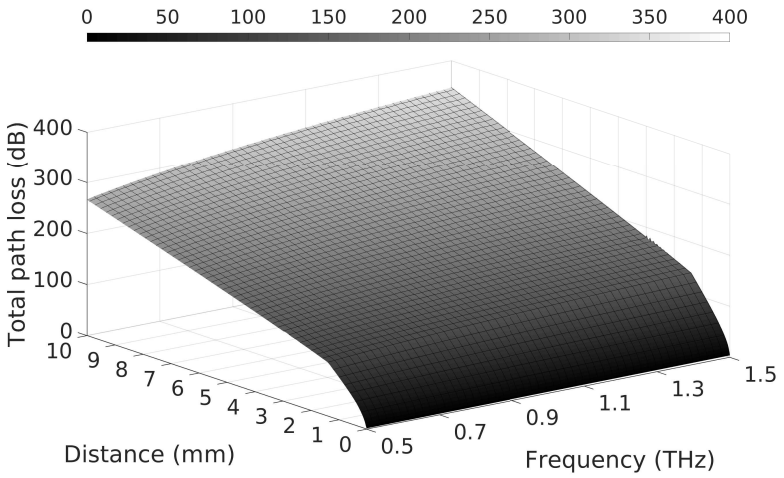

(a) Top-down configuration.

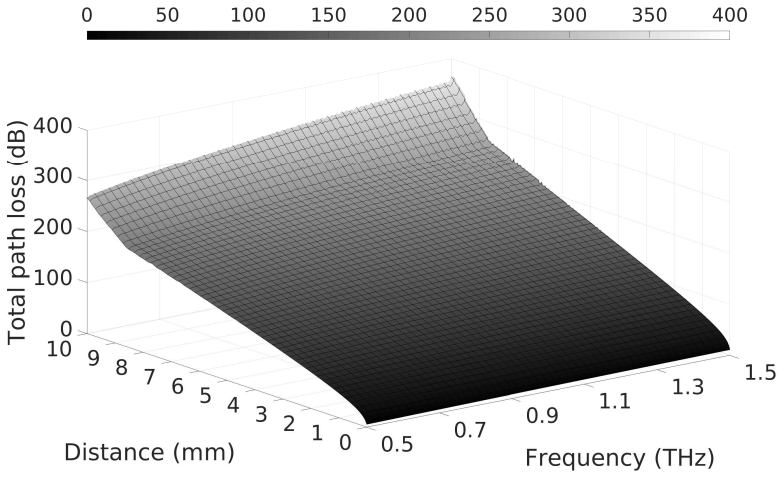

(b) Bottom-up configuration.

Figure 5.7: Total path loss as a function of frequency and transmission range.

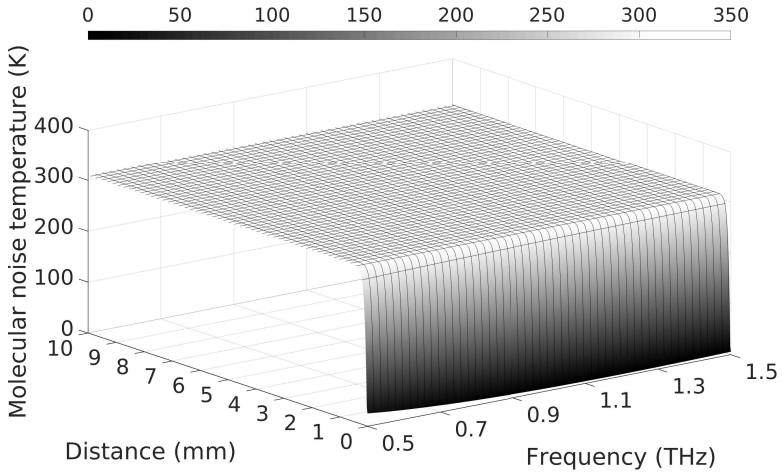

(a) Top-down configuration.

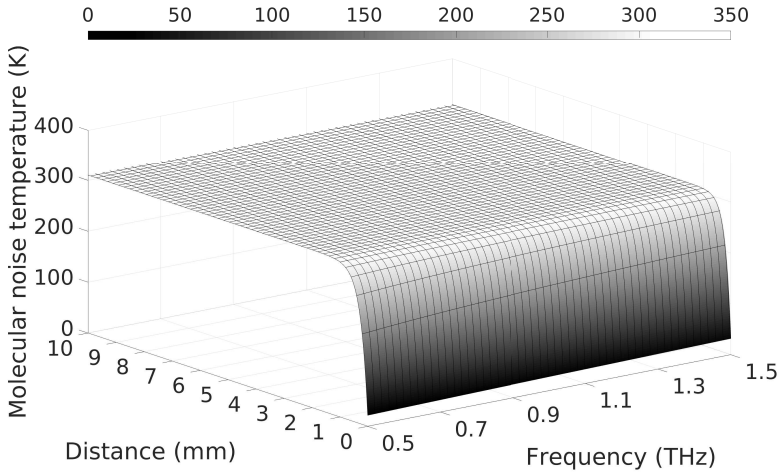

(b) Bottom-up configuration.

Figure 5.8: Molecular absorption noise temperature as a function of frequency and transmission range.

of millimeters, the equivalent molecular noise temperature is not very high, reaching maximum values approximately equal to 310 K (see Figure 5.8). The bounded level of the equivalent noise temperature suggests that a communication link, with a tolerable signal to noise ratio, can be established among transmitter and receiver located inside and outside the human tissues at the Terahertz band.

5.2.4.5 Noise power spectral density

Starting from the equivalent noise temperature $T_{eq}(\omega, z)$, it is possible to evaluate the noise power spectral density, i.e., $N(\omega, z)$, as reported below:

$$N(\omega, z) = k_B T_{eq}(\omega, z), \tag{5.23}$$

where k_B is the Boltzmann constant (i.e., $k_B = 1.380658 \times 10^{-23} J/K$).

Now, by assuming a transmission bandwidth equal to B, the noise power registered at the receiver side, i.e., $P_n(\omega, z)$, is evaluated as:

$$P_n(\omega, z) = \int_B N(\omega, z) df = k_B \int_B T_{eq}(\omega, z) df \tag{5.24}$$

It is evident how the molecular noise increases with communication frequency and transmission distance. This also suggests that it is highly frequency-selective, therefore non-white.

5.3 Transmission techniques

At the nanoscale, the communication capacity is strictly influenced by the transmission strategy and the adopted configuration (i.e., top-down and bottom-up configurations). Regarding the transmission strategies, this book chapter considers three approaches that differently distribute the transmitted power in the frequency domain. They are: flat, pulse-based, and optimal transmission schemes.

Thanks to the strong selectivity of the nanoscale communication channel, the SNR and the resulting upper bound of the channel capacity can only be evaluated by dividing the total bandwidth B into many narrow sub-bands lasting Δf, where the channel is non-selective in the frequency domain. Let $S(\omega_i, z)$ be the transmitted signal power spectral density of the generic

transmission in the i-th sub-band centered at the frequency ω_i at a distance z from the transmitter. The SNR for the i-th sub-band at a distance d, i.e., $SNR(\omega_i, z)$, can be computed as:

$$SNR(\omega_i, z) = \frac{S(\omega_i, z)}{A(\omega_i, z)N(\omega_i, z)}, \tag{5.25}$$

where $A(\omega_i, z)$ is the total channel path loss and $N(\omega_i, z)$ is the noise power spectral density.

According to the Shannon theorem, the upper bound of the resulting channel capacity is equal to:

$$\begin{aligned} C(z) &= \sum_i \Delta f \log_2 \left[1 + SNR(\omega_i, z)\right] = \\ &= \sum_i \Delta f \log_2 \left[1 + \frac{S(\omega_i, z)}{A(\omega_i, z)N(\omega_i, z)}\right]. \end{aligned} \tag{5.26}$$

As demonstrated before, the total path loss $A(\omega_i, z)$ and the noise power spectral density $N(\omega_i, z)$ are influenced by the communication frequency and the distance between transmitter and receiver. On the contrary, the signal power spectral density $S(\omega_i, z)$ is influenced by the adopted transmission strategy. As a result, the channel capacity is strictly influenced by the adopted transmission strategy as well.

5.3.1 Transmission strategies

In nanoscale communications, the information is generally encoded by using short pulses spread over a large bandwidth. The scientific literature considers the TS-OOK as a promising modulation technique for the nanoscale, able to ensure both high energy and communication efficiency [4] [6]. With TS-OOK, a logical 1 is encoded as a short pulse and a logical 0 is encoded as a silence. Moreover, the time interval between two consecutive pulses is much longer than the pulse duration. Consequently, two important advantages are ensured: the nano-devices have not to be synchronized; the medium can be shared among multiple users without risk of collisions.

In what follows, let $B = f_M - f_m$ be the total available bandwidth, where f_m and f_M are the lower and the higher operative frequencies, respectively. When a pulse is transmitted, an amount of power P_{tx} is distributed in the

frequency domain according to the three transmission strategies described below.

5.3.1.1 Flat communication

Flat communication represents the simplest technique, where the transmitted power P_{tx} is uniformly distributed in the frequency domain. In this case, the transmitted power spectral density is:

$$S_{flat}(\omega, z) = \begin{cases} S_0 = \dfrac{P_{tx}}{B} & f_m \leq f \leq f_M \\ 0 & otherwise \end{cases} \tag{5.27}$$

5.3.1.2 Optimal communication

Differently from the previous case, the optimal communication scheme optimally distributes the transmission power within the operative bandwidth in order to maximize the channel capacity. Specifically, the signal power spectral density is computed by solving the optimization problem:

$$maximize \left\{ \sum_i \Delta f \log_2 \left[1 + \frac{S_{opt}(\omega_i, z)}{A(\omega_i, z) N(\omega_i, z)} \right] \right\} \tag{5.28}$$

by jointly taking into account the following three constraints:

1. The total transmission power, expressed as the sum of the signal power spectral density for each sub-bands multiplied by the sub-channel width Δf, cannot exceed the maximum available power over the entire bandwidth P_{tx}:
$$\sum_{i \in \Omega} S_{opt}(\omega_i, z) \Delta f \leq P_{tx}; \tag{5.29}$$

2. The power in a single sub-band should be a fraction, γ, of the total transmission power:
$$S_{opt}(\omega_i, z) \Delta f \leq \gamma P_{tx} \quad \forall i \in \Omega, \gamma \in]0, 1]\,; \tag{5.30}$$

3. The chosen transmission sub-channels must be adjacent:
$$\Omega = \{ i | i_{min_\Omega} \leq i \leq i_{max_\Omega} \}\,. \tag{5.31}$$

The optimization problem formulated in Eq. (5.28) can be solved by using the method of Lagrange multipliers. First of all, by considering the first constraint, the optimization problem can be expressed as:

$$\max\left\{\sum_i \Delta f\left(\log_2\left[1+\frac{S_{opt}(\omega_i,z)}{A(\omega_i,z)N(\omega_i,z)}\right]+\lambda S_{opt}(\omega_i,z)\right)-P_{tx}\right\} \quad (5.32)$$

where λ is the Lagrange multiplier. To find the maximum value, the derivative of the argument of Eq. (5.32) with respect to $S_{opt}(\omega_i, z)$ is put equal to zero, thus obtaining:

$$\ln(2)[S_{opt}(\omega_i,z)+A(\omega_i,z)N(\omega_i,z)]=\lambda^{-1} \quad \forall i \quad (5.33)$$

As a consequence, the overall channel capacity is maximized when:

$$S_{opt}(\omega_i,z)=\beta-A(\omega_i,z)N(\omega_i,z), \quad (5.34)$$

where β is a constant value which can be computed by means of an iterative procedure, following the water-filling principle. In particular, at the n-th step, β is equal to:

$$\beta(n)=\frac{1}{L(n)}\left[\frac{P_{tx}}{\Delta f}+\sum_i A(\omega_i,z)N(\omega_i,z)\right], \quad (5.35)$$

where $L(n)$ is the number of sub-bands at the n-th step. In details, to evaluate $L(n)$ value, the signal power spectral density $S_{opt}(\omega_i, z)$ is computed by considering Eq. (5.34): if $S_{opt}(\omega_i, z) \leq 0$, the corresponding value is set to 0 and the considered sub-band is excluded for the following iterative cycles. The procedure can be stopped when there are no other sub-bands with a negative $S_{opt}(\omega_i, z)$ value. At the end, the total signal power appears optimally distributed in the sub-bands which experience better channel conditions.

It is important to remark that, due to the monotonic behavior of the total path loss, as demonstrated in the previous Section, the selected sub-bands are already adjacent and, consequently, the third constraint is intrinsically respected.

5.3.1.3 Pulse-based communication

Flat and optimal transmission schemes are ideal approaches. Nanotechnology (and in particular graphene-based nano-antennas), instead, allows the transmission of pulses having gaussian shapes in the time domain. Let $p(t) = \frac{1}{s\sqrt{2\pi}} e^{-(t-\mu)^2/(2s^2)}$ be a Gaussian-based pulse, where μ is its mean value and s is the related standard deviation. The pulse-based communication approach models the transmitted pulse through the n-th derivative of $p(t)$, whose representation in the frequency domain is:

$$\phi^{(n)}(\omega, z) = (2\pi f)^{2n} e^{(-2\pi s f)^2} \tag{5.36}$$

Thus, the signal power spectral density of the n-th time derivative is still Gaussian-shaped and could be described as:

$$S^{(n)}_{pulse}(\omega, z) = a_0^2 \phi^{(n)}(\omega, z) = a_0^2 (2\pi f)^{2n} e^{(-2\pi s f)^2}, \tag{5.37}$$

where a_0 is a normalizing constant to adjust the pulse total energy, which is obtained as $a_0^2 = P_{tx} / \int_{f_m}^{f_M} \phi(\omega, z) df$.

Figure 5.9 shows examples of Gaussian-based pulses, obtained by setting n in the range from 1 to 3. Note that, while the pulse duration remains constant (i.e., equal to $100 fs$), the number of oscillations grows up with the derivative order n.

5.4 Analysis of physical transmission rates and communication ranges

In line with [1, 3, 4, 32, 33], and [34], the performance of a nanoscale communication system are evaluated by assuming that the pulse energy and the pulse duration are equal to 500 pJ and 100 fs, respectively. Thus, the resulting amount of power for each transmitted pulse is set to $P_{tx} = 500$ pJ/100 fs $= 5$ kW. When the pulse-based communication strategy is evaluated, the derivative order n of the Gaussian pulse is chosen in the range from 1 to 3 (as already shown before). Whereas, its standard deviation s is set to 0.15.

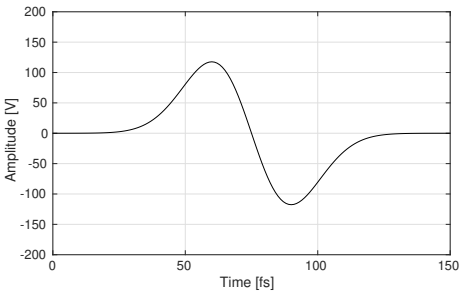

(a) n=1

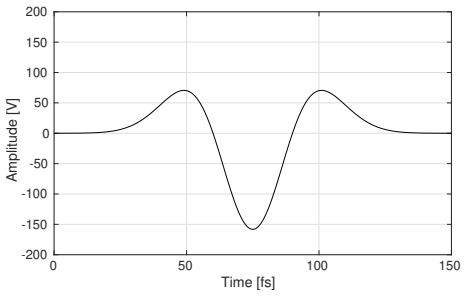

(b) n=2

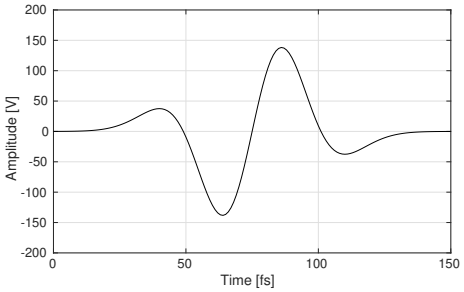

(c) n=3

Figure 5.9: Examples of pulses generated with the Pulse-based communication scheme.

5.4.1 SNR

Figure 5.10 and Figure 5.11 show the SNR estimated for top-down and bottom-up configurations, respectively. First of all, it is possible to observe that these configurations show a common behavior. In both cases, accordingly to the total path loss trend, the SNR grows up when the communication frequency and the distance between source and destination node decrease. On the other hand, given the distance from the source node, the bottom-up configuration registers higher values of SNR than the top-down approach. This is again justified through the total path loss behavior: the inner layers of the stratified medium introduce lower path loss than the outer ones. This anticipates that the direction of the communication in human tissues influences the resulting link capacity.

Furthermore, by taking into account different communication schemes, the behavior of flat and pulse-based transmission strategies is not completely the same, and this will bring to different values of the communication capacity (as illustrated later). Moreover, the study of the optimal transmission scheme brings to two important considerations. First, it is possible to note that the SNR can be evaluated only for a limited portion of the bandwidth, based on the power profile solution of the optimization problem. Second, the adoption of the optimal power profile brings to SNR values that slightly reduces with the distance between communicating nodes, while maintaining similar values in the frequency domain.

5.4.2 Channel capacity

The upper bound of the channel capacity, obtained according to Eq. (5.26), is depicted in Figure 5.12 and Figure 5.13. Also in this case, several differences can be observed between top-down and bottom-up configurations. As already envisioned, given the distance from the source node, the bottom-up direction ensures higher channel capacity. On the other hand, in any case, the channel capacity decreases with the transmission range. This clearly highlights the destroying effect of the path loss, which is even more evident when the distance between transmitter and receiver increases.

As expected, the optimal transmission scheme reaches optimal performance. At the same time, the more realistic approach, based on the transmission of Gaussian-based pulses, generally achieves the lowest performance, which in turn get worse when the derivative order n of the Gaussian-based

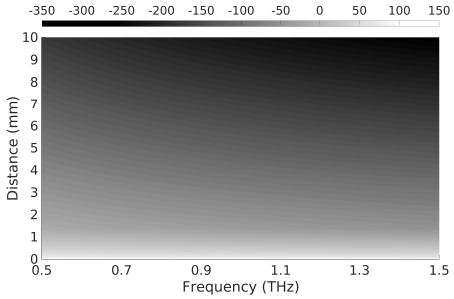

(a) Flat transmission

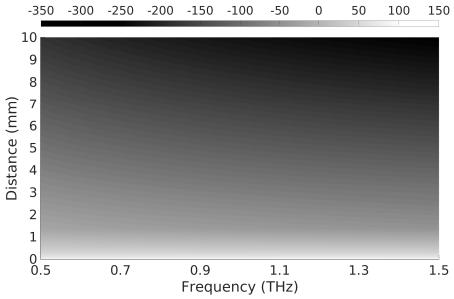

(b) Pulse-based transmission, n=1

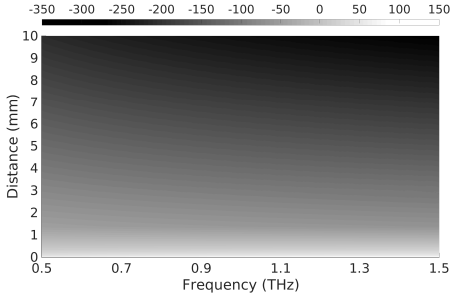

(c) Pulse-based transmission, n=2

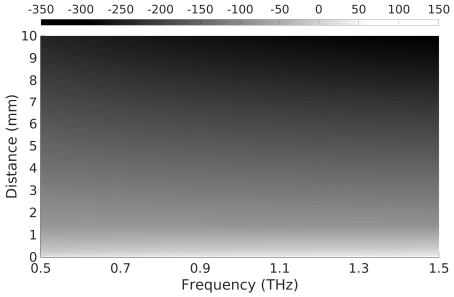

(d) Pulse-based transmission, n=3

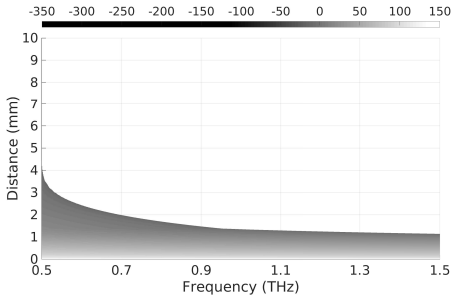

(e) Optimal transmission

Figure 5.10: SNR obtained for the top-down configuration, by varying the transmission strategies.

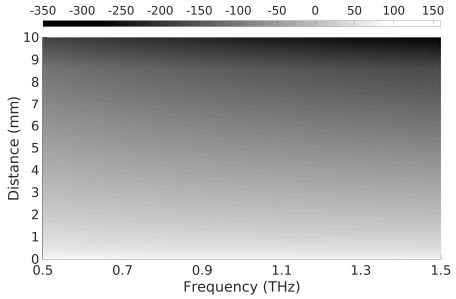

(a) Flat transmission

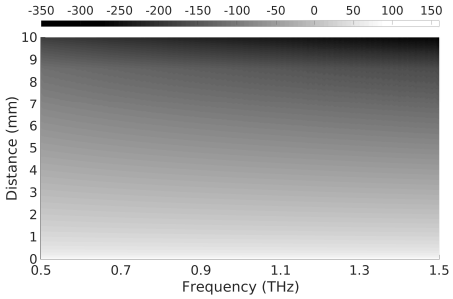

(b) Pulse-based transmission, n=1

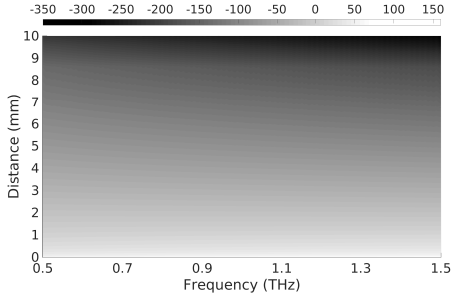

(c) Pulse-based transmission, n=2

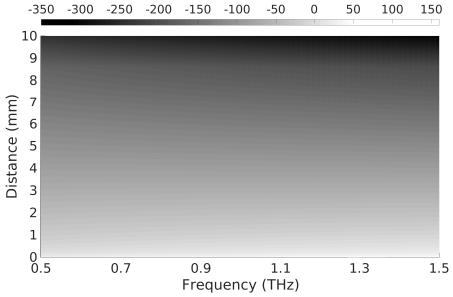

(d) Pulse-based transmission, n=3

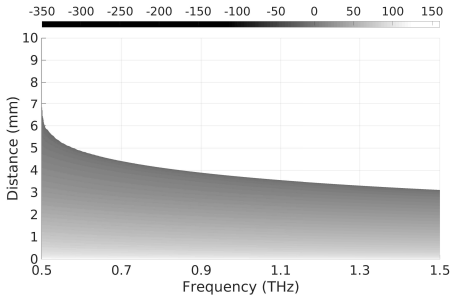

(e) Optimal transmission

Figure 5.11: SNR obtained for the bottom-up configuration, by varying the transmission strategies.

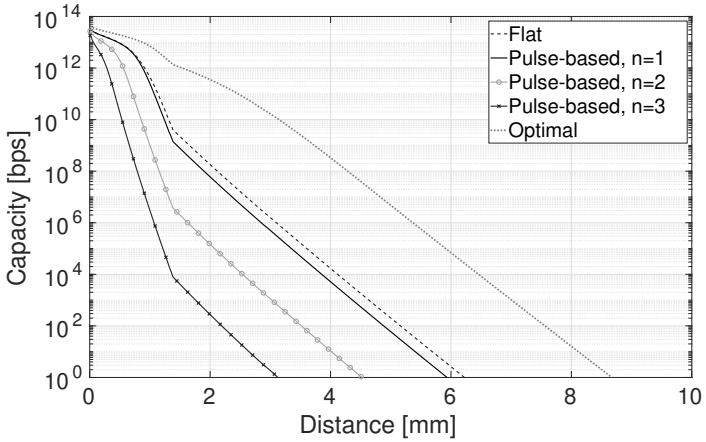

Figure 5.12: Channel capacity as a function of the transmission range, evaluated for the top-down configuration.

pulse increases. In summary, it is possible to conclude that a channel capacity in the order of Tbps can be only reached for transmission ranges less than 2 mm and 4 mm when the top-down and the bottom-up configuration are considered, respectively. Furthermore, when the distance between the source node and the destination device exceeds 9 mm (top-down) and 9.5 mm (bottom-up), communication capabilities are extremely injured (i.e., the channel capacity becomes lower than 1 bps).

5.5 Summary

This book chapter investigated physical transmission rates and communication ranges reachable in human skin. To this end, a sophisticated channel model taking into account the spatial dependence of the skin permittivity has been formulated. Indeed, electromagnetic field and the Poynting vector were calculated by using the FDTD technique, while path loss, noise power spectral density, and SNR were evaluated as a function of the communication frequency and the distance between transmitter and receiver. Starting from these models, physical transmission rates and communication ranges have been calculated by varying the transmission techniques and the positions of both transmitter and receiver. The obtained results demonstrate that a physical data rate in the order of Tbps can be only reached for transmission

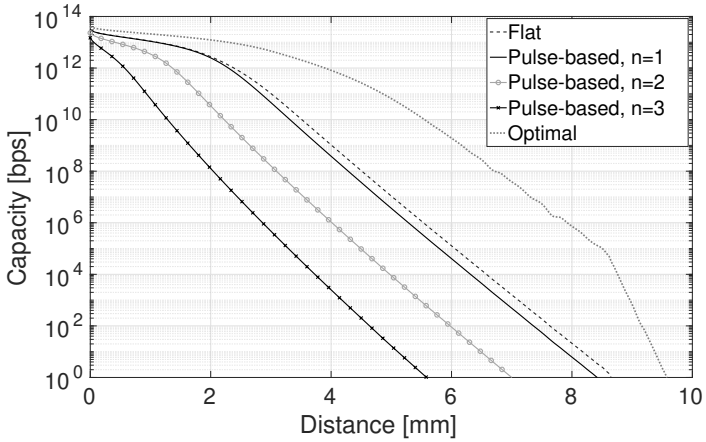

Figure 5.13: Channel capacity as a function of the transmission range, evaluated for the bottom-up configuration.

ranges less than 2 mm. When the distance between transmitter and receiver exceeds 9 mm, communication capabilities are extremely impaired (i.e., the physical data rate tends to be lower than 1 bps). These important findings are extremely useful to drive future research activities devoted to the design of innovative networking methodologies, protocols, and algorithms for the nanoscale.

References

[1] J. M. Jornet and I. F. Akyildiz, "Channel modeling and capacity analysis for electromagnetic wireless nanonetworks in the terahertz band," *IEEE Transactions on Wireless Communications*, vol. 10, no. 10, pp. 3211 –3221, Oct. 2011.

[2] B. Atakan, O. Akan, and S. Balasubramaniam, "Body area nanonetworks with molecular communications in nanomedicine," *IEEE Communications Magazine*, vol. 50, no. 1, pp. 28–34, Jan. 2012.

[3] G. Piro, G. Boggia, and L. A. Grieco, "On the design of an energy-harvesting protocol stack for Body Area Nano-NETworks," *Nano Communication Networks Journal, Elsevier*, vol. 6, no. 2, pp. 74–88, Jun 2015.

[4] J. M. Jornet and I. F. Akyildiz, "Graphene-based plasmonic nano-antenna for terahertz band communication in nanonetworks," *IEEE Journal on Selected Areas in Communications*, vol. 31, no. 12, pp. 685–694, Dec. 2013.

[5] I. F. Akyildiz, C. Han, and S. Nie, "Combating the distance problem in the millimeter wave and terahertz frequency bands," *IEEE Communications Magazine*, vol. 56, no. 6, pp. 102–108, June 2018.

[6] J. M. Jornet and I. F. Akyildiz, "Information capacity of pulse-based wireless nanosensor networks," in *Proc. of IEEE Conf. on Sensor, Mesh and Ad Hoc Communications and Networks, SECON*, Jun. 2011, pp. 80 –88.

[7] D. Caratelli, L. Mescia, P. Bia, and O. V. Stukach, "Fractional-calculus-based FDTD algorithm for ultrawideband electromagnetic characteriza-

tion of arbitrary dispersive dielectric materials," *IEEE Trans. Antennas Propag.*, vol. 64, pp. 3533–3544, 2016.

[8] P. Bia, D. Caratelli, L. Mescia, R. Cicchetti, G. Maione, and F. Prudenzano, "A novel FDTD formulation based on fractional derivatives for dispersive Havriliak-Negami media," *Signal Processing*, vol. 107, pp. 312–318, 2015.

[9] H. Akiyama and R. Heller, *Bioelectrics*. Springer, Berlin, 2016.

[10] M. L. Yarmush, A. Golberg, G. Sersa, T. Kotnik, and D. Miklavcic, "A novel fdtd formulation based on fractional derivatives for dispersive havriliak-negami media," *Annu. Rev. Biomed. Eng.*, vol. 16, pp. 295–320, 2014.

[11] M. Sustarsic, A. Plochowietz, L. Aigrain, Y. Yuzenkova, N. Z. N, and A. Kapanidis, "Optimized delivery of fluorescently labeled proteins in live bacteria using electroporation," *Histochemistry and Cell Biology*, vol. 142, pp. 113–124, 2014.

[12] S. Movassaghi, M. Abolhasan, J. Lipman, D. Smith, and A. Jamalipour, "Wireless body area networks: A survey," *IEEE Communications Surveys Tutorials*, vol. 16, no. 3, pp. 1658–1686, 2014.

[13] T. Nakano, M. Moore, F. Wei, A. Vasilakos, and J. Shuai, "Molecular communication and networking: Opportunities and challenges," *IEEE Transactions on NanoBioscience*, vol. 11, no. 2, pp. 135–148, Jun. 2012.

[14] G. Piro, P. Bia, G. Boggia, D. Caratelli, L. A. Grieco, and L. Mescia, "Terahertz electromagnetic field propagation in human tissues: a study on communication capabilities," *Nano Communication Networks, Elsevier*, vol. 10, pp. 51–59, 2016.

[15] S. Canovas-Carrasco, A. J. Garcia-Sanchez, and J. Garcia-Haro, "A nanoscale communication network scheme and energy model for a human hand scenario," *Nano Communication Networks, Elsevier*, vol. 15, pp. 17–27, 2018.

[16] R. Magin, *Fractional Calculus in Bioengineering*. Begell House, 2006.

REFERENCES

[17] C. Polk and E. Postow, *Biological Effects of Electromagnetic Fields*. Crc Press, Boca Raton, USA, 19966.

[18] V. Raicu, "Dielectric dispersion of biological matter: Model combining debye-type and "universal" responses," *Physical review. E, Statistical physics, plasmas, fluids, and related interdisciplinary topics*, vol. 60, pp. 4677–80, 1999.

[19] L. Mescia, P. Bia, M. A. Chiapperino, and D. Caratelli, "Fractional calculus based fdtd modeling of layered biological media exposure to wideband electromagnetic pulses," *Electronics*, vol. 6, p. 106, 2017.

[20] P. Bia, D. Caratelli, L. Mescia, and J. Gielis, "Analysis and synthesis of supershaped dielectric lens antennas," *IET Microwaves, Antennas & Propagation*, vol. 9, pp. 1497–1504, 2015.

[21] L. Mescia, P. Bia, and D. Caratelli, "Fractional derivative based FDTD modeling of transient wave propagation in Havriliak-Negami media," *IEEE Trans. Microwave Theory and Techniques*, vol. 62, pp. 1920–1929, 2014.

[22] P. Bia, L. Mescia, and D. Caratelli, "Fractional calculus-based modeling of electromagnetic field propagation in arbitrary biological tissue," *Mathematical Problems in Engineering*, vol. 2016, pp. 1–11, 2016.

[23] L. Mescia, P. Bia, and D. Caratelli, "Fractional-calculus-based electromagnetic tool to study pulse propagation in arbitrary dispersive dielectrics," *Physica Status Solidi A*, 2018.

[24] K. Yang, A. Pellegrini, M. Munoz, A. Brizzi, A. Alomainy, and Y. Hao, "Numerical Analysis and Characterization of THz Propagation Channel for Body-Centric Nano-Communications," *IEEE Transactions on Terahertz Science and Technology*, vol. 5, no. 3, pp. 419–426, May 2015.

[25] K. Sasaki, M. Mizuno, K. Wake, and S. Watanabe, "Measurement of the dielectric properties of the skin at frequencies from 0.5 GHz to 1 THz using several measurement systems," in *Proc. of International Conference on Infrared, Millimeter, and Terahertz waves (IRMMW-THz)*, Hong Kong, August 2015.

[26] M. Ney and I. Abdulhalim, "Does human skin truly behave as an array of helical antennae in the millimeter and terahertz wave ranges ?" *Optics Letters*, vol. 35, pp. 3180–3182, 2010.

[27] S. Naito, M. Hoshi, and S. Yagihara, "Microwave dielectric analysis of human stratum corneum in vivo," *Biochimica et Biophysica Acta*, vol. 1381, pp. 293–304, 1998.

[28] P. Hasgall, F. D. Gennaro, C. Baumgartner, E. Neufeld, M. Gosselin, D. Payne, A. Klingenbock, and N. Kuster. (2015) IT-IS database for thermal and electromagnetic parameters of biological tissues. [Online]. Available: http://www.itis.ethz.ch/database, access done 18/04/2019.

[29] S. Huclova, D. Erni, and J. Frohlich, "Modeling and validation of dielectric properties of human skin in the mhz region focusing on skin layer morphology and material composition," *Journal of Physics D Applied Physics*, vol. 45, 2012.

[30] P. Zakharov, F. Dewarrat, A. Caduff, and M. Talary, "The effect of blood content on the optical and dielectric skin properties," *Physiological measurement*, vol. 32, pp. 131–149, 2011.

[31] L. Mescia, P. Bia, and D. Caratelli, "Fractional-calculus-based FDTD method for solving pulse propagation problems," in *Proc. of IEEE International Conference on Electromagnetics in Advanced Applications (ICEAA)*, Sep. 2015, pp. 460–463.

[32] G. Piro, K. Yang, G. Boggia, N. Chopra, L. A. Grieco, and A. Alomainy, "Terahertz communications in human tissues at the nano-scale for healthcare applications," *IEEE Transactions on Nanotechnology*, vol. 14, no. 3, pp. 404–406, May 2015.

[33] Bush, J. Paluh, G. Piro, V. Rao, V. Prasad, and A. Eckford, "Defining communication at the bottom," *IEEE Transactions on Molecular, Biological, and Multi-Scale Communications (T-MBMC)*, vol. 1, no. 1, pp. 90–96, Aug. 2015.

[34] J. M. Jornet and I. F. Akyildiz, "Joint energy harvesting and communication analysis for perpetual wireless nanosensor networks in the terahertz band," *IEEE Transactions on Nanotechnology*, vol. 11, no. 3, pp. 570–580, May 2012.